Lawrence Berkeley National Laboratory
LBL Publications

Title

Humidity Disrupts Structural and Chiroptical Properties of Chiral 2D Perovskites

Permalink

https://escholarship.org/uc/item/6cp7z900

Journal

ACS Nano, 19(11)

ISSN

1936-0851

Authors

Nurdillayeva, Raushan N
Moral, Raphael F
Pols, Mike
et al.

Publication Date

2025-03-25

DOI

10.1021/acsnano.5c00480

Peer reviewed

ARTICLE

Humidity Disrupts Structural and Chiroptical Properties of Chiral 2D Perovskites

Raushan N. Nurdillayeva,[#] Raphael F. Moral,[#] Mike Pols, Do-Kyoung Lee, Virginia Altoe, Craig P. Schwartz, Shuxia Tao, and Carolin M. Sutter-Fella*

Cite This: https://doi.org/10.1021/acsnano.5c00480

Read Online

ACCESS | Metrics & More | Article Recommendations | Supporting Information

ABSTRACT: Chiral two-dimensional (2D) hybrid organic–inorganic metal halide perovskite semiconductors have emerged as an exceptional material platform with many design opportunities for spintronic applications. However, a comprehensive understanding of changes to the crystal structure and chiroptical properties upon exposure to atmospheric humidity has not been established. We demonstrate phase degradation to the 1D (MBA)PbI$_3$ (MBA = methylbenzylammonium) and the hypothetical (MBA)$_3$PbI$_5$·H$_2$O hydrate phases, accompanied by a reduction and disappearance of the chiroptical response. First-principle simulations show that water molecules preferentially locate at the interface between the organic cations and the inorganic framework, thereby disrupting the hydrogen bonding, impacting both the structural chirality and stability of the material. These findings provide critical insights into phase degradation mechanisms and their impact on chiroptical activity in chiral 2D perovskites.

KEYWORDS: *chiral 2D perovskites, humidity degradation, chiroptical properties, phase transformation, DFT calculations*
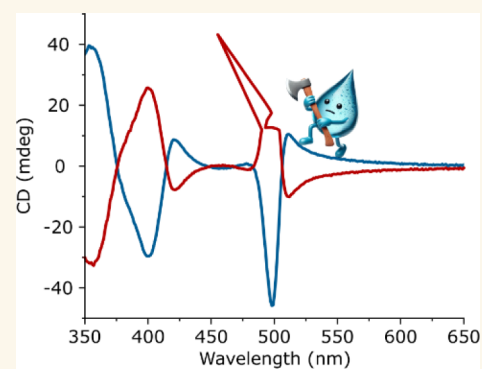
INTRODUCTION

Low-dimensional, specifically two-dimensional (2D), hybrid organic–inorganic metal halide perovskite (2D MHP) semiconductors have attracted intense research attention due to their unique properties. These materials consist of well-defined inorganic metal halide layers sandwiched between bulky organic spacer cations, adopting the Ruddlesden–Popper (RP) crystal structure.[1,2] 2D MHPs exhibit strong light absorption,[3] broad bandgap tunability,[4,5] compositional and structural diversity,[6–8] and strong quantum and dielectric confinement of excitons.[9] Recent discoveries show that the incorporation of chiral organic molecules into 2D MHPs creates chiral semiconductors, allowing control of light, charge, and spin without the need for an external magnetic field.[8,10] Chirality describes an object that cannot be superposed on its mirror image through any combination of rotations and translations,[11] resulting in structures that are compositionally identical but geometrically distinct.

The first reported chiral 2D MHP material, *R*-/*S*-/*rac*-MBA$_2$PbI$_4$ (*R*-/*S*-/*rac*-MBAPI), is based on the chiral organic cations *R*- and *S*-α-methylbenzylammonium, abbreviated as *R*/*S*-MBA (Figure 1a).[12,13] Chiral 2D MHPs exhibit chiro-optical (chiroptical) properties that arise from the interaction between chiral structures and light, leading to different responses to left- and right-circularly polarized light. For example, *R*-/*S*-MBAPI shows circular dichroism (CD), corresponding to the differ-

ential absorption of left- and right-handed circularly polarized light.[14] The transport of charges through chiral structures depends on the charges' spin configuration, and their spin population can be controlled without a magnetic field.[8] Given these properties, there are multiple applications for chiral materials, including chiroptoelectronics,[15–17] quantum computing,[18] and spintronics.[19–21]

Most MHP materials degrade in the presence of humidity. It is critical, therefore, to investigate humidity-induced degradation in new optoelectronic materials, such as chiral 2D perovskites. In comparison to "regular" 2D MHPs, there is an intrinsic structural instability in the chiral counterpart. This instability lies in the steric hindrance imposed by the CH$_3$ group in the α position to the NH$_3^+$ polar head (Figure S1).[22] With few exceptions, where the CH$_3$ group is in the β position to the NH$_3^+$ group,[23] the majority of chiral 2D perovskites share the steric hindrance in the α position. This steric repulsion decreases the penetration depth of the NH$_3^+$ moiety

A
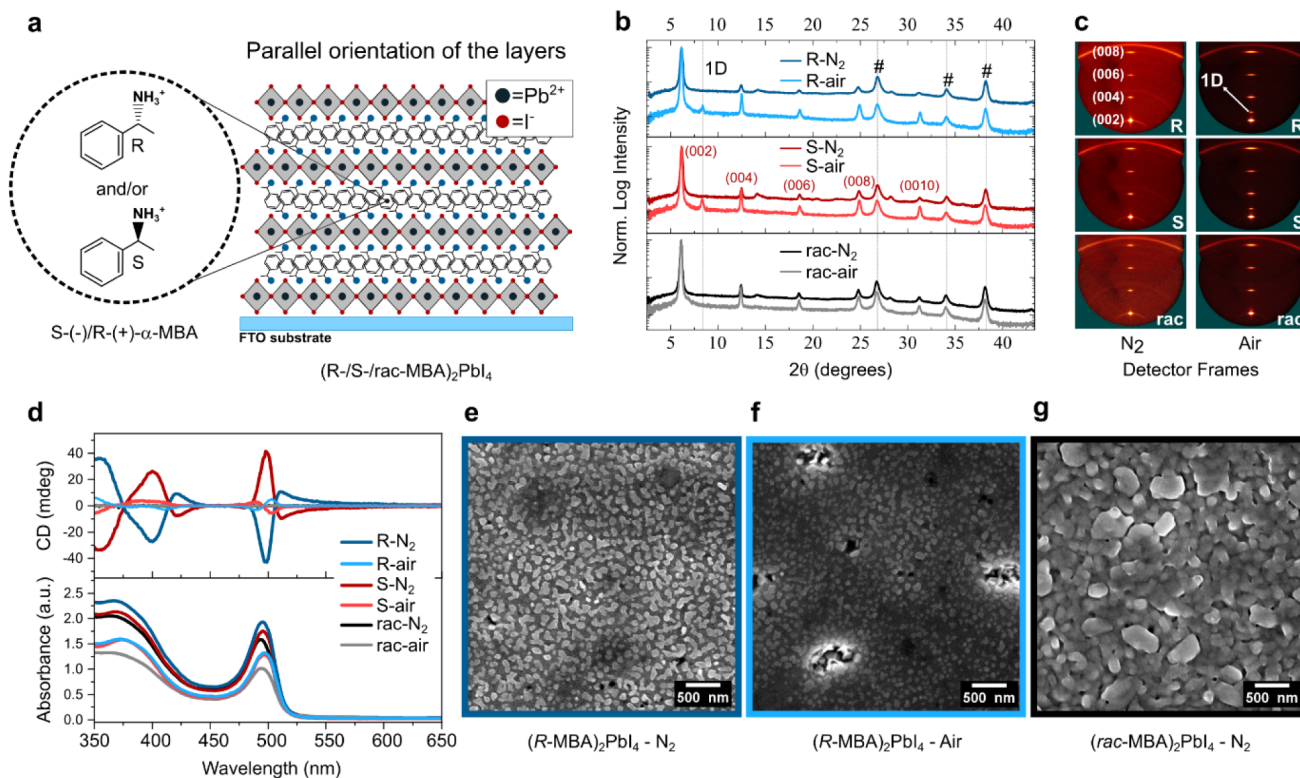
Figure 1. (a) *R*- and *S*-α-methylbenzylamine and schematics of the chiral 2D MHP layers oriented parallel to the substrate. (b) Thin film XRD of homochiral and racemic phases prepared both in the glovebox (GB) and ambient atmosphere (air) - # denotes FTO substrate diffractions. (c) X-ray detector frames showing highly oriented, out-of-plane diffractions and highly textured films for each diffraction pattern in b. (d) Circular dichroism and absorption spectra of the thin films of the homochiral and racemic phases prepared in the GB and air. Scanning electron microscopy (SEM) images of $(R\text{-MBA})_2PbI_4$ with a magnification of 20 kx prepared (e) in the GB and (f) in air; (g) SEM images of the racemic phase prepared in the GB.

in the cationic sites in the inorganic sublattice.[6] Consequently, it imposes an intrinsic instability on the material due to the weakening of the Coulombic interaction and hydrogen bonding between the NH_3^+ polar head and the axial halide anions, which often favors the formation of lower-dimensional phases.[22] This happens for any chiral cation having the CH_3 in the α position to NH_3^+, as evidenced by the competing 1D phase in several chiral 2D perovskites meeting this condition: α-methylbenzylammonium,[10] *p*-methoxy-α-methylbenzylam-monium,[22] 1-(1-naphthyl)ethylammonium,[24] and 1-(2-naphthyl)ethylammonium.[25] Building on this understanding, we investigated the effect of humidity on the structure and chiroptical properties of *R*-/*S*-/*rac*-MBAPI.

Here, we report on the effect of humidity on the structure and chiroptical properties of a model structure, *R*-/*S*-/*rac*-MBAPI. Upon interaction with water molecules, 1D (*R*-/*S*-MBA)PbI$_3$ and hydrate phases form. Such phase degradation is accompanied by a reduction and disappearance of the CD signal. 2D phase degradation is reversible upon reannealing if the hydrate phase forms but irreversible when 1D (MBA)PbI$_3$ forms. DFT calculations show that water molecules preferentially locate at the interface between the organic cations and the inorganic framework, disrupting the hydrogen bonding and impacting the chirality and stability of the chiral phase. Lastly, grazing incidence wide-angle X-ray scattering (GIWAXS) measurements show degradation of the homochiral phases upon exposure to 70% RH through 1D phase formation. Interestingly, GIWAXS depth profile analysis suggests that degradation starts at the material/substrate interface and grain

boundaries, rather than on the film surface. Our findings contribute toward a fundamental understanding of the correlations between chiral 2D MBAPI, humidity, and chiroptical activity. This knowledge is anticipated to be generally relevant for processing other chiral 2D perovskites with steric hindrance at the α-position to the NH_3^+ moiety.

RESULTS AND DISCUSSION

The synthesis of 2D *R*-/*S*-/*rac*-MBAPI thin films starts with the single crystal (Figure S2) preparation, as described in the methods section, followed by spin-coating deposition and annealing. These thin films were fabricated either in a N$_2$-filled glovebox or under an ambient atmosphere (∼53−54% RH) from acetonitrile solutions of the single crystals. Figure 1b shows the X-ray diffraction (XRD) patterns for *R*-/*S*-/*rac*-MBAPI thin films made in different environments, and the corresponding 2D detector images are depicted in Figure 1c. XRD data show that films made in the N$_2$ atmosphere are phase pure with strong parallel orientation of the 2D layers (Figure 1a), as apparent from the intense out-of-plane Bragg reflections in the diffraction frames (Figure 1c). The peak positions match the reference pattern calculated from single crystal data (Figures S3 and S4).[12,13,26] Films made under ambient atmosphere also show oriented diffraction peaks, but the *R*-/*S*-MBAPI show additional 1D phase impurities; i.e., (*R*-/*S*-MBA)PbI$_3$. The appearance of the 1D phase possibly indicates that water is interacting with the solvent/materials during thin film formation, leading to the thermodynamically more stable 1D phase.[27]

The chiroptical response of the materials was characterized by CD measurements. These highly parallel-oriented films may exhibit linear dichroism and linear birefringence (LDLB) due to possible macroscopic anisotropies such as sample orientation-dependent absorption and different refractive indices along different crystallographic axes. To account for these effects, CD data were recorded from the front and back sides of the films, and the genuine CD (CD_{gen}) response, as well as the absorption g-factor, were calculated (Figure S5a, see Methods section).[28] As expected, R-/S-MBAPI films show differential absorption of circularly polarized light, while rac-MBAPI shows a flat line, indicating equal absorption regardless of polarization (Figures 1d and S5a), consistent with previous reports.[10] The CD peaks for R-MBAPI and S-MBAPI are at the same locations with opposite signs, but the peaks for samples made in air are shifted compared to those made in N_2 at the excitonic transitions.[5,29] Although the excitonic absorption of both air and N_2 R-/S-MBAPI films is at approximately the same position (Figure 1d, bottom), the inflection point of the chiroptical response, generated by the Cotton effect, shifts to lower energies for the air samples. The microstructure of the N_2 and air R-MBAPI films is relatively similar (Figure 1e,f), while the rac-MBAPI shows similar crystallites but significantly larger in size (Figure 1g), as revealed by scanning electron microscopy (SEM). While all of the films show pinholes in the SEM images, it is notable that R-MBAPI prepared in air shows craters with bright edges along the film, possibly caused by the reaction of the 2D materials with atmospheric water. This result is in line with the diffractions of the R-MBAPI films in Figure 1b. Cross-sectional SEM images are shown in Figure S6, and they reveal compact and smooth films with thicknesses of approximately 360 and 300 nm for R- and rac-MBAPI, respectively.

Next, we explore the effects of the ambient atmosphere on the atomic-level details of chiral perovskites. Specifically, we examine the impact of H_2O on the structural chirality of R-MBAPI (Figure 2a), using density functional theory (DFT) calculations. The simulations indicate that water molecules preferentially adsorb at the interface between the chiral organic cations (R-MBA$^+$) and the inorganic framework ([PbI$_6$]$^{4-}$), as shown in Figure 2b, with additional details shown in Note S1 and Figure S7. Here, H_2O can form strong hydrogen bonds with the NH$_3^+$ head groups of the cations (N—H···O) and the I$^-$ halide anions (O—H···I) (Figure 2c). In doing so, the water molecules disrupt the hydrogen bonding between the chiral organic cations and the inorganic framework, possibly facilitating conversion from the chiral 2D perovskite into the 1D or hydrate phases.

We then identify the impact of the H_2O molecules on the structural chirality of R-MBAPI. To do so, we make use of the descriptors for chiral distortions in the inorganic framework that were introduced by Pols et al.[30] In particular, we make use of the descriptor to characterize the structural chirality of the inorganic framework in the in-plane direction ($\epsilon_{MX_4}^{\parallel}$), by probing the helicity of the lead halide (Pb—I) bonds (Figure S8). A detailed explanation of how this descriptor is determined can be found in Note S2. The structural chirality of the inorganic framework of R-MBAPI ($\epsilon_{MX_4}^{\parallel} = -8.1 \times 10^{-3}$) decreases whenever an H_2O molecule is incorporated into the structure ($\epsilon_{MX_4}^{\parallel} = -5.6 \times 10^{-3}$). We speculate that the reduced structural chirality of the inorganic framework, from which the
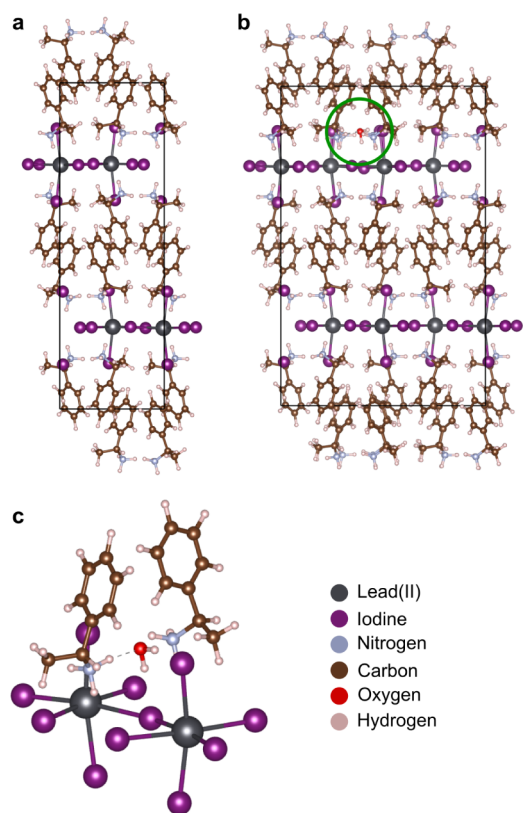
Figure 2. Side view of the crystal structure of (a) pristine (R-MBA)$_2$PbI$_4$ and (b) (R-MBA)$_2$PbI$_4$ with a H_2O molecule embedded in the structure (green circle). (c) The H_2O molecule binds to both the organic cations (N—H···O bonds) and the inorganic framework (O—H···I). Purple spheres represent iodine; dark gray, lead; light blue, nitrogen; brown, carbon; and light magenta, hydrogen atoms.

chiral optical signal stems, contributes to the reduction of the degree of the selective adsorption of circularly polarized light. Together with the changes in the perovskite phase upon water adsorption (e.g., 2D phase converted into 1D or hydrate phases), these effects could explain the differences in the CD measurements in Figure 1d.

Next, we investigated the effect of aging under ambient conditions (~53–54% RH) on the crystal structure and chiroptical response. XRD patterns of fresh and aged R-MBAPI and rac-MBAPI, respectively, initially show peaks attributed to phase-pure 2D phases, followed by a loss of the 2D structure at the expense of 1D, hydrate, or PbI$_2$ phases (Figure 3a,b; see Figure S9 for full-range diffractograms). Interestingly, the homochiral phase degrades differently than the racemic one. We observe PbI$_2$ and hydrate phase formation in the latter case, as opposed to 1D and hydrate phase formation in the homochiral material.

We propose that upon humidity exposure in the dark, a hydrate of R-/S-/rac-MBAPI is formed. This iodine-based hydrate phase has not been reported yet, but hydrate structures for Br/Cl phases[13] (for the racemic materials) support our hypothesis. For the Br/Cl hydrate phases, the calculated powder diffraction patterns (Figure S10) show the main diffraction (200) at $2\theta = 6.06°$ and 6.13°, respectively. This suggests that the d-spacing for the hydrates is very similar to that of the 2D phases. Analyzing the hydrate structures (Figure S11) reveals that water molecules disrupt the 2D layers
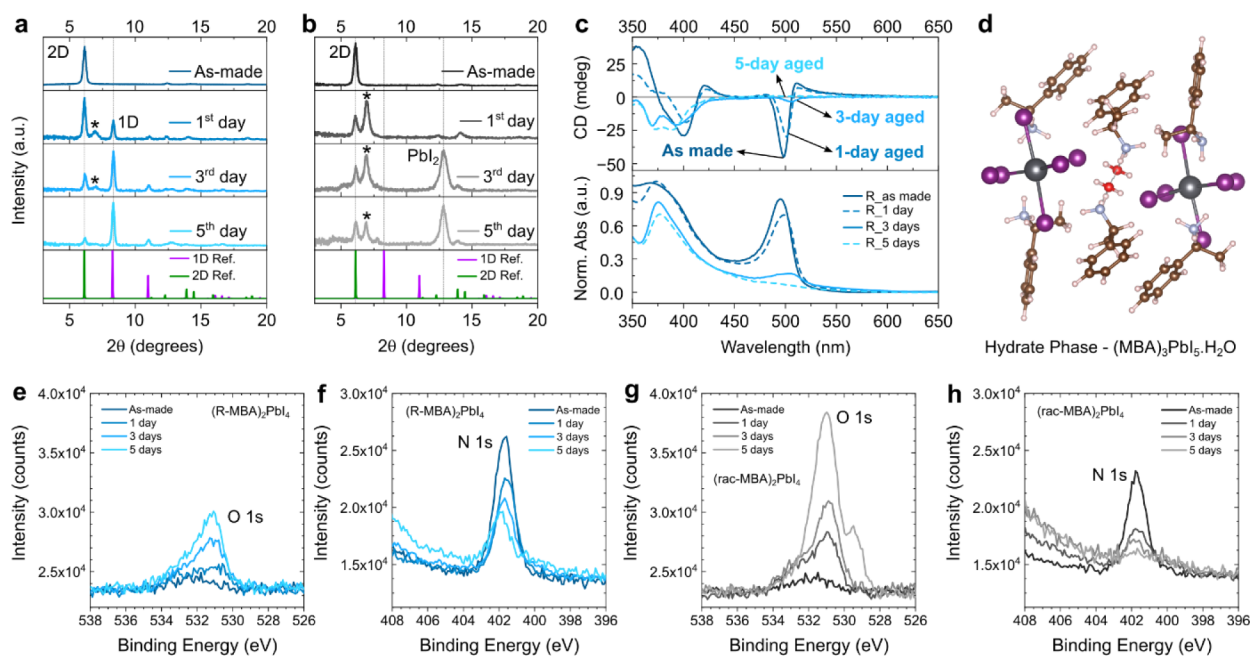
Figure 3. Effect of humidity as a function of exposure time to ambient atmosphere (as-made, 1-day, 3-day, and 5-day aged). Thin-film XRD patterns for as-made and aged samples along with the reference XRD for 2D and 1D phases (a) $(R\text{-MBA})_2PbI_4$ and (b) $(rac\text{-MBA})_2PbI_4$ - (*) denotes the hydrate phase; (c) circular dichroism curves along with the absorption spectra of $(R\text{-MBA})_2PbI_4$ thin films for as-made and aged samples; (d) DFT-optimized iodine-based hydrate phase showing the disruption of the $[PbI_6]^{4-}$ octahedra layers by the adsorption of water molecules; (e-h) surface-sensitive XPS spectra of O 1s and N 1s levels before and after exposure to ambient atmosphere. $(R\text{-MBA})_2PbI_4$ and $(rac\text{-MBA})_2PbI_4$ samples are shown.

without significantly altering the bilayer of MBA$^+$ cations, maintaining a d-spacing comparable with the original 2D phase. We hypothesize that a similar reaction occurs during the hydration of iodine-based materials, leading to a diffraction peak at $2\theta = 6.97°$. Utilizing the Br hydrate as a template, we simulated a crystal structure for a possible iodine-based hydrate (Figure S11). We observe an increase in the d-spacing with the addition of a larger halide anion, and the main diffraction is at $2\theta = 5.99°$ (Figure S10, blue curve). Again, the proximity of the d-spacing of this simulated structure supports the hypothesis of hydrate formation in the case of $rac\text{-MBAPI}$.

In analogy with 3D MHP films, water molecules infiltrate the perovskite structure and form hydrate perovskite phases.[31−33] Generally, organic−inorganic hybrid perovskite crystals are characterized by ionic interactions between the two components and hydrogen-bonding interactions between the NH$_3^+$ polar moiety and the halide anions.[34] Hydrate phase formation in CH$_3$NH$_3$PbI$_3$ was hypothesized to occur when water molecules form a stronger hydrogen-bonding interaction than the one with NH$_3^+$.[32] This weakens the organic cation-PbI$_6$ bond and, consequently, enables deprotonation of the organic cation and its volatilization as a neutral amine (e.g., methylamine). Additionally, water protonates iodide, leading to the formation of volatile HI (hydroiodic acid).[35] Here, we hypothesize that water reacts similarly, and the degradation mechanism differs slightly for rac- compared to that of R-MBAPI. For the homochiral phases, the hydrate phase appears to act as an intermediate during the transition from 2D to 1D phases. This is evidenced by the rapid evolution of the 1D phase diffraction at $2\theta = 8.3°$ and the weak diffraction of the hydrate at $2\theta = 6.97°$ (Figure 3a). In this scenario, the hydrate phase induces the deprotonation of the MBA$^+$ cation and the formation of HI, leading to the 1D phase formation:

$$(S-/R-MBA)_2PbI_{4(s)} \xrightarrow{H_2O} (S-/R-MBA)PbI_{3(s)}$$
$$+ MBA^0_{(g)} + HI_{(g)}$$
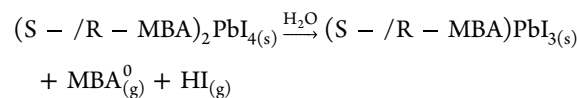
where MBA^0 stands for the neutral amine after deprotonation. The S-MBAPI homochiral phase shows a similar degradation pathway, as expected (Figure S12).

For the racemic phase, the hydrate evolves at the expense of the 2D phase but is more persistent than in homochiral analogs. Even after prolonged exposure, no 1D phase diffraction was observed. After 3 days of air exposure, PbI$_2$ is visible as a degradation phase. Thus, for the racemic material, hydration and proton exchange reactions seem to drive the formation of the PbI$_2$ directly from the 2D phase:

$$(rac-MBA)_2PbI_{4(s)} \xrightarrow{H_2O} PbI_{2(s)} + 2MBA^0_{(g)} + 2HI_{(g)}$$

We note that the 1D phase $(rac\text{-MBA})PbI_3$ has been reported in the literature;[13] however, under our experimental conditions, the results show no evidence that the degradation mechanism of 2D $rac\text{-MBAPI}$ involves the formation of its 1D phase.

We also tested humidity-induced phase reversibility, where a fresh film was exposed to ambient humidity for 1 day followed by annealing in an N$_2$ atmosphere. While the hydrate phase is reversible and disappears upon annealing, the concentration of the 1D phase (as a degradation phase of the R-MBAPI) does increase compared to the 2D phase upon aging and reannealing (Figure S13). This observation suggests that this diffraction appearing at $2\theta = 6.97°$ is indeed from the hydrate phase. The formation of volatile MBA and/or HI prevents the reversibility of the 1D to 2D phase.

The CD of the aged R-MBAPI films exhibits a reduction in intensity, disappearance of CD peaks, and a change in peak
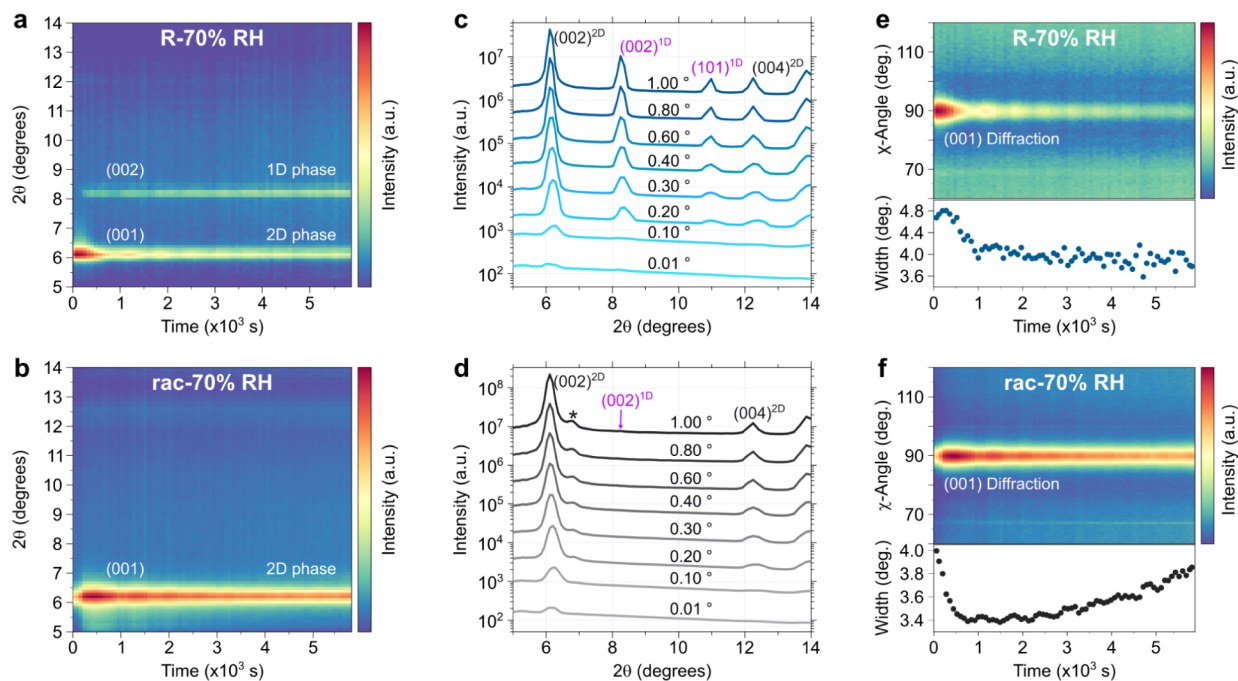
Figure 4. (a) - (b) False-color diffraction maps of *R*- and (*rac*-MBA)$_2$PbI$_4$ films on FTO-coated glass substrates showing the material aging under humidity exposure (70% RH) for approximately 1.5 h; (c) - (d) azimuthally integrated diffraction patterns of *R*- and rac-(MBA)$_2$PbI$_4$ with incidence angle variation from α = 0.01° to 1.0° - the asterisk in d evidence the hydrate phase (pink labels are from the 1D phase diffractions); (e) - (f) χ-angle integration of the (002) diffraction of 2D *R*- and (*rac*-MBA)$_2$PbI$_4$ phases over time under humidity exposure (70% RH for 1.5 h).

position. The CD peak position follows the excitonic absorption band visible around ∼500 nm in the absorbance spectra (Figure 3c). As the excitonic absorption becomes weaker, the CD response decreases. With the appearance of the 1D and hydrate phases, the CD response is weaker, and the films look clearly degraded (see photographs in Figure S14). Another piece of evidence of degradation and thickness reduction of the films, due to the mass loss, is the more intense FTO diffractions in the aged films compared to the as-made ones (Figures S9 and S12). The disappearance of the CD signal at the excitonic absorption supports our hypothesis of water molecules disrupting the inorganic sublattice, depleting the excitonic states, typical of the 2D framework of corner-sharing [PbI$_6$]$^{4-}$ octahedra (Figure 3d).

Surface-sensitive X-ray photoelectron spectroscopy (XPS) measurements were conducted on the *R*- and *rac*-MBAPI samples, as prepared and after exposure to the ambient atmosphere, to assess elemental composition at the surface (Figures 3e−h and S15). Table S3 summarizes the relative elemental composition of the films normalized by the Pb 4f signal, assuming that Pb^{2+} species are the least likely to leave the film or migrate in the material under study. While the fresh films show a negligible signal for the O 1s signal, it increases upon exposure to humidity and oxygen (Figure 3e−g). The main difference was found for the N 1s signal (Figure 3f−h). It almost disappears for *rac*-MBAPI but does not decrease as much for *R*-MBAPI. This is consistent with the XRD results discussed above because, in the *R*-MBAPI sample, we primarily found 1D phase formation, which means that there is only partial N loss. In the *rac*-MBAPI sample, we found a significant amount of PbI$_2$, meaning a nearly complete loss of the organic molecules and therefore a substantial reduction in the N 1s signal.

To assess where the 2D phase decomposition happens during degradation and across the film thickness, we performed in situ GIWAXS measurements at 70% RH (Figure 4). Fresh *R*-/*rac*-MBAPI films were loaded into the humidity chamber under N$_2$ flow (RH < 1%); then, the RH was increased to 70% while measuring GIWAXS at an incidence angle of α = 0.01° for 90 min. With this incidence angle, we probed only a few nanometers below the surface (∼3 nm). The 1D phase diffraction becomes apparent on the surface of the *R*-MBAPI film within the first 5 min of measurement, revealing a high sensitivity of the homochiral phases to moisture. On the contrary, the racemic phase does not show any change on the surface of the material except for a decrease in the diffraction intensity. Ahn et al. verified that, in controlled conditions (25 °C and 20% RH), the films of homochiral *R*-/*S*-MBAPI are fairly stable, retaining the same structural properties for 7 days.[10] Ma et al. found no change in the diffraction pattern of the materials after aging their single crystals for 67 days.[36] In contrast, our experiments reveal a high sensitivity of homochiral and *rac*-MBAPI thin films to moisture, with 1D or hydrate phases appearing within 1 day in ambient atmosphere (∼53−54% RH) and within a few minutes in 70% RH. Ishii and Miyasaka tested the thermal and environmental stability of (R/S-1NEA)$_2$PbBr$_4$ and (R/S-2NEA)$_2$PbBr$_4$, with 1/2NEA being 1-1- and 1-(2-naphthyl)-ethylammonium cations, respectively.[25] Both chiral 2D MHPs maintained good structural stability under ambient conditions for several weeks. However, at 75% relative humidity (RH) and 75 °C, (R/S-1NEA)$_2$PbBr$_4$ lost its structure and CD response, also forming its 1D phase, while (R/S-2NEA)$_2$PbBr$_4$ retained its 2D structure for longer due to stronger hydrogen bonding.[25] This hydration susceptibility has been reported for similar achiral materials.[37−40] Dučinskas et al., for instance, found that Dion-Jacobson phase 2D perovskites are also very

susceptible to hydration.[37,38] Interestingly, the structure based on 1,4-phenylenedimethylammonium, a double cationic species, also forms a 1D phase upon hydration. This hydration is reversible with an additional annealing step, at the cost of a crystallinity decrease and lower photoluminescence intensity.[38]

To verify internal changes in the materials, we measured GIWAXS at different incidence angles from α = 0.01 to 1.0° after the humidity exposure (Figure S16 shows the q-space plots before and after exposure). Remarkably, both films (R-/rac-MBAPI) exhibit a nearly pure 2D phase on the surface after aging. Only upon increasing incidence angles (α > 0.1°), the hydrate and 1D phases become more evident (Figure 4c,d). Again, the homochiral phases tend to form the 1D phase, while the racemic phase tends to form the hydrate phase. The peak intensity of the impurity phases increases with an increasing incidence angle, suggesting that the 2D phase degradation does not initiate at the surface of the films.

It has been reported for 3D MHP solar cells that degradation under ambient conditions and solar spectrum illumination can initiate from either the electron or hole transport layer/perovskite interface.[41] The degradation of the chiral 2D MHPs is likely initiated at the grain boundaries and the material-substrate interface rather than at the surface. This is attributed to the higher hydrophobicity of the surface, which is terminated with MBA$^+$ cations, as indicated by the time-of-flight secondary ion mass spectrometry (ToF-SIMS) analysis of 2D perovskites.[42−45] Additionally, as shown in Figure 1e−g, all films exhibit pinholes that may allow water molecules to reach more hydrophilic sites within the material. Throughout the degradation process, we do not observe any significant change in the texture of the films, as can be seen from the plots of intensity distribution over the χ-angle (Figure 4e,f). The intensity of the diffraction rings reaches the maximum at 90°; i.e., in the out-of-plane direction, in agreement with Figure 1c. The fwhm of these peaks is very narrow ($\Delta\chi \sim 4°$), demonstrating the highly uniform planar texture of these materials. Therefore, achieving smooth surfaces (Figure S6), highly oriented crystalline films (Figures 1c and S16), and pinhole-free fabrication could be effective strategies to enhance the stability of chiral 2D perovskite films.

CONCLUSION

In summary, we found that homochiral phases tend to degrade into the (R-/S-MBA)PbI$_3$ 1D phase in the presence of moisture, while the racemic analog preferentially forms a hydrate phase with a hypothetical (MBA)$_3$PbI$_5$·H$_2$O stoichiometry, as extracted from the simulated crystalline structure. This hydrate phase further degrades into PbI$_2$, and its crystal structure has yet to be reported in the literature. The degradation is more likely to initiate at the grain boundaries and material-substrate interface due to the higher hydrophobicity of the surface terminated MBA$^+$ cations. First-principles simulations show that water molecules preferentially locate at the interface between the organic cations and the inorganic framework, thereby disrupting the hydrogen bonding and impacting the chiroptical properties and stability of the material. The hydration of these materials is reversible upon annealing; however, the transition from the 2D to the 1D phase is irreversible due to the loss of one equivalent of α-methylbenzylamine and HI. Our findings indicate that chiral 2D MHPs are highly sensitive to humidity, with degradation occurring in less than a day under ambient conditions and within minutes at 70% RH. This sensitivity to stressors like humidity is associated with the steric effect of the methyl group in the α-position relative to the NH$_3^+$ polar moiety and, therefore, common to the majority of chiral 2D perovskites. Our findings are crucial for guiding the application of these materials in chiroptoelectronic devices, particularly regarding humidity exposure and fabrication in ambient environments. The presence of 1D and hydrate phases, which are more insulating, can also disrupt charge carrier mobility in such devices.

METHODS

Materials. Racemic α-methylbenzylamine (99%), S-(−)-α-methylbenzylamine (98%), and R-(+)-α-methylbenzylamine (98%) were purchased from Sigma-Aldrich. Lead(II) oxide (99.99% metals basis) was purchased from Thermo Scientific Chemicals. Hydroiodic acid (HI, 57 wt % in H$_2$O, distilled, stabilized, 99.95%) was purchased from Sigma-Aldrich. Acetonitrile (99.9%, gradient grade, suitable for HPLC) was purchased from Sigma-Aldrich. All the chemicals were used as received. FTO substrates (15 Ohm/sq conductivity) were purchased from Automatic Research GmbH.

Single Crystal Synthesis. In a 20 mL vial, 200 mg of PbO (0.9 mmol) is dissolved in 5 mL of hydroiodic acid (Sigma, 57 wt % in H$_2$O, stabilized) at 110 °C on a hot plate in a fume hood. After complete dissolution, 200 μL of rac-, S-, or R-α-methylbenzylamine (1.55 mmol) dissolved in 500 μL of hypophosphorous acid (H$_3$PO$_2$) is added to the mixture dropwise. The flask is then loosely capped and stirred at 110 °C in a silicone oil bath at 1000 rpm to yield a clear yellow solution. The temperature is then decreased from 110 to 20 °C at a rate of 4 °C per hour (hot plate Torrey Pines Scientific, model HS70). After this time, roughly 1 cm long orange needles of (R-/S-/rac-MBA)$_2$PbI$_4$ are formed. The needles of the racemic phase are smaller than those of their homochiral analogues.

This synthesis can also be made without a heating ramp, using regular hot plate equipment. In the absence of a heating controller, after obtaining a clear yellow solution, the flask is transferred to a silicone oil bath at ∼110 °C under stirring at 1000 rpm. Subsequently, the temperature of the bath is lowered to ∼90 °C, and the mixture stays at this temperature for 30 min. After this time, the stirring is stopped, and the temperature of the bath is lowered to ∼75 °C for another hour. Then, the temperature is lowered to ∼45 °C, and the reaction mixture is left at this temperature overnight. The next day, needle-shaped single crystals (SC) should be visible. Finally, the temperature is lowered at a rate of 5 °C every 30 min until room temperature. Fast cooling may lead to contamination with the 1D phase.

To wash the SCs, the supernatant is removed with the help of a disposable pipette, and then a volume of neat toluene, enough to cover the SCs, is added. The SCs are washed with 40 mL of neat toluene in portions of approximately 5 mL each time. When approximately 20 mL of toluene is used, the single crystals are transferred to a clean vial with the help of a disposable spatula. After using 40 mL of toluene, the SCs are washed with a mixture of 15 mL of toluene and 5 mL of diethyl ether (3:1) in portions of approximately 4 mL each time. This mixture is important to remove excess HI from the SCs. When this mixture is used, the solvent becomes slightly yellow, possibly from etching the surface of the SCs. After washing with this solvent mixture, the SCs are washed with another 12 mL of neat toluene to remove any diethyl ether residue. The

SCs are then dried in a vacuum oven overnight at 60 °C and kept in an N_2-filled glovebox until their use. Yield: (rac-MBA)$_2$PbI$_4$ = 62%; (S-/R-MBA)$_2$PbI$_4$ = 50% (based on Pb mol ratio).

Thin Film Preparation. Thin films are prepared with 150 mM solutions prepared with the previously synthesized single crystals. 72 mg of (R-/S-/rac-MBA)$_2$PbI$_4$ (0.075 mmol) is dissolved in 500 μL of acetonitrile and allowed to stir until fully dissolved. This concentration is close to saturation for the racemic material, so gentle heat of ~60 °C is necessary to dissolve the single crystals. FTO substrates are cleaned with DI water, acetone, and IPA in a sonicator bath for at least 15 min with each solvent. The substrates are dried with a N_2 flow and allowed to dry overnight in an oven at 60 °C. Before using them to coat the films, they are treated with UV-ozone for 30 min. We used 40 μL of the precursor solutions to coat the films. The spinning configuration is 10 s at 1000 rpm/500 rpm·s^{-1}, and then 30 s at 4000 rpm/1000 rpm·s^{-1}. After the spin-coat step, the films are immediately annealed at 65 °C for 10 min.

Thin Film X-ray Diffraction. XRD measurements were performed using a Bruker AXS D8-Discover X-ray diffractometer. The source used was Co Kα radiation (λ = 1.7902 Å). All the diffractograms were reported after converting the wavelength to the more commonly used Cu Kα radiation (λ = 1.5406 Å). The measurements were carried out with a Bragg−Brentano geometry with an area detector. The initial incidence and detection angles were 5° and 15°, respectively. The whole measurement was performed with three frames, where the source and detector increased by 5°/frame each, with ending positions at 15° and 25°, respectively. Because the 2D layers present a parallel orientation to the surface of the substrate, we observed strong out-of-plane diffractions in the X-ray detector. For these measurements, we set the sample stage to oscillate in a way that the films moved 4 mm in the x and 4 mm in the y directions while measuring. This way, we could obtain an averaged signal of a larger area of the films. The integration time for each frame was 600 s (a total of 1800 s for the whole measurement).

Grazing-Incidence X-ray Wide-Angle Scattering (GI-WAXS). GIWAXS measurements were carried out at the 7.3.3 SAXS/GISAXS beamline at the advanced light source (ALS) at Lawrence Berkeley National Laboratory. The X-ray energy was 10 keV with a beam horizontal size of ~0.5 mm. At grazing-incidence angles, the beam spreads over the sample in a line larger than the substrate (fluorine-doped tin oxide on glass—FTO 15 × 15 mm^2). The sample-to-detector distance was 280 mm. The detector used was a Pilatus 1 M with a pixel size of 0.172 × 0.172 mm^2. For all of the samples, an exposure time of 0.2 s was used. The ambient humidity was ~45% during the experiment. In the humidity chamber, the relative humidity (RH) was lower than 1% with constant N_2 flow. We controlled the humidity with Linkan equipment attached to a Teflon chamber with Kapton windows. The chamber is capable of keeping the RH with a variation of ±5%. To avoid the horizontal gaps between the modules of the Pilatus 1 M detector, we measured two scans in slightly different z-positions (ca. 50 μm difference) and generated a composite general binary image without these lines. All experiments were measured this way. We varied the incidence angle from α = 0.01° to 1.0°, depending on the measurement. Data reduction and treatment were performed using the Irina[46] and Nika[47] macros for IgorPro software and custom-made Python scripts.

Circular Dichroism (CD) and Genuine CD (CD$_{gen}$) Calculations. CD measurements were carried out using a J-815 Jasco spectropolarimeter. To allow for linear dichroism and linear birefringence (LDLB) corrections, we measured the films facing the source (front) and then flipped them to measure the other side (back). For this correction, we used the equation CD$_{gen}$ = 0.5 (CD$_{front}$ + CD$_{back}$), where CD$_{gen}$ stands for "genuine" CD. For each CD curve, we used a window from 300 to 700 nm with steps of 1 nm. The integration time at each wavelength was 1 s, and each curve was an average of three measurements. To calculate the g_{factor} (or dissymmetry factor, an absolute number that ranges from −2 to +2) in absorbance units (A.U.), we used the absorption spectra from the same instrument. The g_{factor} curves were calculated using the equation: g_{factor} = $\Delta A/(A*32982)$, where ΔA is the differential absorption of circularly polarized light from the CD spectrum, A is the absorbance, and 32982 is a correction factor to convert g_{factor} to A.U. (1 A.U. = 32982 mdeg).[28]

X-ray Photoelectron Spectroscopy (XPS). X-ray photoelectron spectra were acquired using a Thermo Fisher K-Alpha$^+$ XPS instrument (using the Avantage software) equipped with a focused monochromatic Al Kα X-ray excitation source (1486.7 eV), a collection lens with a 30° half an gle acceptance, and a hemispherical analyzer with a multichannel detector at normal incidence to the sample. The X-ray spot size is 400 μm. The analysis chamber pressure was maintained at ~1.0×10^{-7} mBar during data acquisition. Perovskite films on ITO substrates were mechanically fastened to standard specimen mounts, and the analysis was performed on as-made samples as well as after aging in air for 1, 3, and 5 days. Fresh samples were transferred from the glovebox and loaded in the XPS prechamber in less than 5 min. The binding energies obtained in the XPS analysis were calibrated using the C 1s (C−C peak at 284.8 eV) as a charge reference. Spectral peaks were fitted using the CasaXPS software version 2.3.19PR1.0 from Casa Software Ltd. (US).

DFT Calculations. The perovskite structures were optimized with density functional theory (DFT) calculations using the projector-augmented wave (PAW) method as implemented in the Vienna Ab-initio Simulation Package (VASP).[48,49,50,51] The outermost electrons of H (1s^1), C (2s^{2}2p^2), N (2s^{2}2p^3), O (2s^{2}2p^4), I (5s^{2}5p^5), and Pb (6s^{2}6p^2) were treated as valence electrons. The exchange-correlation interaction of the electrons was modeled using the Perdew, Burke, and Ernzerhof (PBE) functional.[52] Dispersion interactions were included through the DFT-D3 scheme with Becke-Johnson damping introduced by Grimme et al.[53] The plane wave basis set was expanded to 500 eV. An energy and force convergence criterion of 10^{-5} eV and 10^{-2} eV·A^{-1} were used, respectively.

The structures of (R-MBA)$_2$PbI$_4$ and hydrate (rac-MBA)$_3$PbI$_5$·H$_2$O were optimized by allowing the atom positions, cell axes, and cell shape to change. To investigate the impact of water (H$_2$O) molecules on the structural chirality of the chiral perovskites, a 2 × 2 × 1 supercell of (R-MBA)$_2$PbI$_4$ was created by expanding it in the lateral x- and y-directions and inserting a H$_2$O molecule. The water molecules were placed in different locations; i.e., far away from and close to the inorganic layers to scan the preferential adsorption sites for H$_2$O. The structures were subsequently optimized by only allowing the atom positions to change. The dimensions of the optimized geometries, the Γ-centered k-meshes used during their optimization, and adsorption enthalpies are shown in

Table S3. Additional details of the structural models can be found in Note S1 and Figure S7.

Scanning Electron Microscopy. Scanning electron microscopy (SEM) images were measured using a Zeiss Gemini Ultra-55 Analytical SEM instrument with a 5 kV accelerating voltage and a magnification of 20 kx. The films were mounted on aluminum stubs (Ted Pella, Inc.) with copper tape connected to the surface to avoid charging effects. For cross-section analysis, Au sputtering was carried out on the surface of the samples to reduce the charging effect.

ASSOCIATED CONTENT

Ⓢ Supporting Information

The Supporting Information is available free of charge at https://pubs.acs.org/doi/10.1021/acsnano.5c00480.

> Additional figures and schematics, additional X-ray diffraction data, additional circular dichroism data, additional SEM data, additional details on the DFT calculations and chiral descriptors, additional GIWAXS data (PDF)

AUTHOR INFORMATION

Corresponding Author

Carolin M. Sutter-Fella − *Molecular Foundry, Lawrence Berkeley National Laboratory, Berkeley, California 94720, United States;* ⓘ orcid.org/0000-0002-7769-0869; Email: csutterfella@lbl.gov

Authors

Raushan N. Nurdillayeva − *Molecular Foundry, Lawrence Berkeley National Laboratory, Berkeley, California 94720, United States; Khoja Akhmet Yassawi International Kazakh-Turkish University, Turkistan 161200, Kazakhstan;* ⓘ orcid.org/0000-0001-9444-737X

Raphael F. Moral − *Molecular Foundry, Lawrence Berkeley National Laboratory, Berkeley, California 94720, United States; Nevada Extreme Conditions Laboratory, University of Nevada, Las Vegas, Las Vegas, Nevada 89154, United States;* ⓘ orcid.org/0000-0002-1844-4035

Mike Pols − *Materials Simulation & Modelling, Department of Applied Physics and Science Education, Eindhoven University of Technology, Eindhoven 5600 MB, Netherlands;* ⓘ orcid.org/0000-0002-1068-9599

Do-Kyoung Lee − *Molecular Foundry, Lawrence Berkeley National Laboratory, Berkeley, California 94720, United States; Nevada Extreme Conditions Laboratory, University of Nevada, Las Vegas, Las Vegas, Nevada 89154, United States*

Virginia Altoe − *Molecular Foundry, Lawrence Berkeley National Laboratory, Berkeley, California 94720, United States*

Craig P. Schwartz − *Nevada Extreme Conditions Laboratory, University of Nevada, Las Vegas, Las Vegas, Nevada 89154, United States;* ⓘ orcid.org/0000-0002-4149-2684

Shuxia Tao − *Materials Simulation & Modelling, Department of Applied Physics and Science Education, Eindhoven University of Technology, Eindhoven 5600 MB, Netherlands;* ⓘ orcid.org/0000-0002-3658-8497

Complete contact information is available at:
https://pubs.acs.org/10.1021/acsnano.5c00480

Author Contributions

#R.N.N. and R.F.M. contributed equally to this work.

Notes

The authors declare no competing financial interest.

REFERENCES

(1) Stoumpos, C. C.; Cao, D. H.; Clark, D. J.; Young, J.; Rondinelli, J. M.; Jang, J. I.; Hupp, J. T.; Kanatzidis, M. G. Ruddlesden−Popper Hybrid Lead Iodide Perovskite 2D Homologous Semiconductors. *Chem. Mater.* **2016**, *28* (8), 2852−2867.

(2) Grancini, G.; Nazeeruddin, M. K. Dimensional Tailoring of Hybrid Perovskites for Photovoltaics. *Nat. Rev. Mater.* **2019**, *4* (1), 4−22.

(3) Yaffe, O.; Chernikov, A.; Norman, Z. M.; Zhong, Y.; Velauthapillai, A.; van der Zande, A.; Owen, J. S.; Heinz, T. F. Excitons in Ultrathin Organic-Inorganic Perovskite Crystals. *Phys. Rev. B* **2015**, *92* (4), 045414.

(4) Weidman, M. C.; Seitz, M.; Stranks, S. D.; Tisdale, W. A. Highly Tunable Colloidal Perovskite Nanoplatelets through Variable Cation, Metal, and Halide Composition. *ACS Nano* **2016**, *10* (8), 7830−7839.

(5) Ahn, J.; Ma, S.; Kim, J.-Y.; Kyhm, J.; Yang, W.; Lim, J. A.; Kotov, N. A.; Moon, J. Chiral 2D Organic Inorganic Hybrid Perovskite with Circular Dichroism Tunable Over Wide Wavelength Range. *J. Am. Chem. Soc.* **2020**, *142* (9), 4206−4212.

(6) Li, X.; Hoffman, J. M.; Kanatzidis, M. G. The 2D Halide Perovskite Rulebook: How the Spacer Influences Everything from the Structure to Optoelectronic Device Efficiency. *Chem. Rev.* **2021**, *121* (4), 2230−2291.

(7) Smith, M. D.; Connor, B. A.; Karunadasa, H. I. Tuning the Luminescence of Layered Halide Perovskites. *Chem. Rev.* **2019**, *119* (5), 3104−3139.

(8) Lu, H.; Vardeny, Z. V.; Beard, M. C. Control of Light, Spin and Charge with Chiral Metal Halide Semiconductors. *Nat. Rev. Chem.* **2022**, *6* (7), 470−485.

(9) Mao, L.; Stoumpos, C. C.; Kanatzidis, M. G. Two-Dimensional Hybrid Halide Perovskites: Principles and Promises. *J. Am. Chem. Soc.* **2019**, *141* (3), 1171−1190.

(10) Ahn, J.; Lee, E.; Tan, J.; Yang, W.; Kim, B.; Moon, J. A New Class of Chiral Semiconductors: Chiral-Organic-Molecule-Incorporat-

ing Organic−Inorganic Hybrid Perovskites. *Mater. Horiz.* **2017**, *4* (5), 851−856.

(11) Favre, H. A.; Powell, W. H. IUPAC Compendium of Chemical Terminology. In *Nomenclature of Organic ChemistryNomenclature of Organic Chemistry*, 3rd ed.; The Royal Society of Chemistry: 2013; p 479. DOI :.

(12) Billing, D. G. Bis(1-Phenylethylammonium) Tetraiodoplumbate(II). *Acta Crystallogr., Sect. E:Struct. Rep. Online* **2002**, *58* (11), m669−m671.

(13) Billing, D. G.; Lemmerer, A. Synthesis and Crystal Structures of Inorganic−Organic Hybrids Incorporating an Aromatic Amine with a Chiral Functional Group. *CrystEngcomm* **2006**, *8* (9), 686−695.

(14) Greenfield, J. L.; Wade, J.; Brandt, J. R.; Shi, X.; Penfold, T. J.; Fuchter, M. J. Pathways to Increase the Dissymmetry in the Interaction of Chiral Light and Chiral Molecules. *Chem. Sci.* **2021**, *12* (25), 8589−8602.

(15) Chen, C.; Gao, L.; Gao, W.; Ge, C.; Du, X.; Li, Z.; Yang, Y.; Niu, G.; Tang, J. Circularly Polarized Light Detection Using Chiral Hybrid Perovskite. *Nat. Commun.* **2019**, *10* (1), 1927.

(16) Dang, Y.; Liu, X.; Cao, B.; Tao, X. Chiral Halide Perovskite Crystals for Optoelectronic Applications. *Matter* **2021**, *4* (3), 794−820.

(17) Long, G.; Sabatini, R.; Saidaminov, M. I.; Lakhwani, G.; Rasmita, A.; Liu, X.; Sargent, E. H.; Gao, W. Chiral-Perovskite Optoelectronics. *Nat. Rev. Mater.* **2020**, *5* (6), 423−439.

(18) Humphreys, P. C.; Kalb, N.; Morits, J. P. J.; Schouten, R. N.; Vermeulen, R. F. L.; Twitchen, D. J.; Markham, M.; Hanson, R. Deterministic Delivery of Remote Entanglement on a Quantum Network. *Nature* **2018**, *558* (7709), 268−273.

(19) Naaman, R.; Paltiel, Y.; Waldeck, D. H. Chiral Molecules and the Electron Spin. *Nat. Rev. Chem.* **2019**, *3* (4), 250−260.

(20) Lee, H.; Lee, C. U.; Yun, J.; Jeong, C.-S.; Jeong, W.; Son, J.; Park, Y. S.; Moon, S.; Lee, S.; Kim, J. H.; Moon, J. A Dual Spin-Controlled Chiral Two-/Three-Dimensional Perovskite Artificial Leaf for Efficient Overall Photoelectrochemical Water Splitting. *Nat. Commun.* **2024**, *15* (1), 4672.

(21) Wang, J.; Lu, H.; Pan, X.; Xu, J.; Liu, H.; Liu, X.; Khanal, D. R.; Toney, M. F.; Beard, M. C.; Vardeny, Z. V. Spin-Dependent Photovoltaic and Photogalvanic Responses of Optoelectronic Devices Based on Chiral Two-Dimensional Hybrid Organic−Inorganic Perovskites. *ACS Nano* **2021**, *15* (1), 588−595.

(22) Scalon, L.; New, A.; Ge, Z.; Mondal, N.; Campos, R. D.; Quarti, C.; Beljonne, D.; Nogueira, A. F.; Bakulin, A. A.; Vaynzof, Y. Understanding and Controlling the Photoluminescence Line Shapes of 2D Perovskites with Chiral Methylbenzylammonium-Based Cations. *Chem. Mater.* **2024**, *36* (9), 4331−4342.

(23) Huang, P.-J.; Taniguchi, K.; Miyasaka, H. Bulk Photovoltaic Effect in a Pair of Chiral−Polar Layered Perovskite-Type Lead Iodides Altered by Chirality of Organic Cations. *J. Am. Chem. Soc.* **2019**, *141* (37), 14520−14523.

(24) Ishii, A.; Miyasaka, T. Direct Detection of Circular Polarized Light in Helical 1D Perovskite-Based Photodiode. *Sci. Adv.* **2020**, *6* (46), No. eabd3274.

(25) Son, J.; Ma, S.; Jung, Y.-K.; Tan, J.; Jang, G.; Lee, H.; Lee, C. U.; Lee, J.; Moon, S.; Jeong, W.; Walsh, A.; Moon, J. Unraveling Chirality Transfer Mechanism by Structural Isomer-Derived Hydrogen Bonding Interaction in 2D Chiral Perovskite. *Nat. Commun.* **2023**, *14* (1), 3124.

(26) Marchenko, E. I.; Fateev, S. A.; Petrov, A. A.; Korolev, V. V.; Mitrofanov, A.; Petrov, A. V.; Goodilin, E. A.; Tarasov, A. B. Database of Two-Dimensional Hybrid Perovskite Materials: Open-Access Collection of Crystal Structures, Band Gaps, and Atomic Partial Charges Predicted by Machine Learning. *Chem. Mater.* **2020**, *32* (17), 7383−7388.

(27) Scalon, L.; Brunner, J.; Guaita, M. G. D.; Szostak, R.; Albaladejo-Siguan, M.; Kodalle, T.; Guerrero-León, L. A.; Sutter-Fella, C. M.; Oliveira, C. C.; Vaynzof, Y.; Nogueira, A. F. Tuning Phase Purity in Chiral 2D Perovskites. *Adv. Opt. Mater.* **2024**, *12* (2), 2300776.

(28) Albano, G.; Pescitelli, G.; Bari, L. D. Chiroptical Properties in Thin Films of π-Conjugated Systems. *Chem. Rev.* https://pubs.acs.org/doi/10.1021/acs.chemrev.0c00195.

(29) Georgieva, Z. N.; Bloom, B. P.; Ghosh, S.; Waldeck, D. H. Imprinting Chirality onto the Electronic States of Colloidal Perovskite Nanoplatelets. *Adv. Mater.* **2018**, *30* (23), 1800097.

(30) Pols, M.; Brocks, G.; Calero, S.; Tao, S. Temperature-Dependent Chirality in Halide Perovskites. *J. Phys. Chem. Lett.* **2024**, *15* (31), 8057−8064.

(31) Boyd, C. C.; Cheacharoen, R.; Leijtens, T.; McGehee, M. D. Understanding Degradation Mechanisms and Improving Stability of Perovskite Photovoltaics. *Chem. Rev.* **2019**, *119* (5), 3418−3451.

(32) Christians, J. A.; Miranda Herrera, P. A.; Kamat, P. V. Transformation of the Excited State and Photovoltaic Efficiency of CH₃NH₃PbI₃ Perovskite upon Controlled Exposure to Humidified Air. *J. Am. Chem. Soc.* **2015**, *137* (4), 1530−1538.

(33) Marchezi, P. E.; Therézio, E. M.; Szostak, R.; Loureiro, H. C.; Bruening, K.; Gold-Parker, A.; Melo, M. A.; Tassone, C. J.; Tolentino, H. C.; Toney, M. F.; et al. Degradation Mechanisms in Mixed-Cation and Mixed-Halide $Cs_xFA_{1-x}Pb(Br_yI_{1-y})_3$ Perovskite Films under Ambient Conditions. *J. Mater. Chem. A* **2020**, *8* (18), 9302−9312.

(34) Quarti, C.; Grancini, G.; Mosconi, E.; Bruno, P.; Ball, J. M.; Lee, M. M.; Snaith, H. J.; Petrozza, A.; De Angelis, F. The Raman Spectrum of the CH₃NH₃PbI₃ Hybrid Perovskite: Interplay of Theory and Experiment. *J. Phys. Chem. Lett.* **2014**, *5* (2), 279−284.

(35) Frost, J. M.; Butler, K. T.; Brivio, F.; Hendon, C. H.; van Schilfgaarde, M.; Walsh, A. Atomistic Origins of High-Performance in Hybrid Halide Perovskite Solar Cells. *Nano Lett.* **2014**, *14* (5), 2584−2590.

(36) Ma, J.; Fang, C.; Chen, C.; Jin, L.; Wang, J.; Wang, S.; Tang, J.; Li, D. Chiral 2D Perovskites with a High Degree of Circularly Polarized Photoluminescence. *ACS Nano* **2019**, *13* (3), 3659−3665.

(37) Dučinskas, A.; Fish, G. C.; Hope, M. A.; Merten, L.; Moia, D.; Hinderhofer, A.; Carbone, L. C.; Moser, J.-E.; Schreiber, F.; Maier, J.; Milić, J. V.; Grätzel, M. The Role of Alkyl Chain Length and Halide Counter Ion in Layered Dion−Jacobson Perovskites with Aromatic Spacers. *J. Phys. Chem. Lett.* **2021**, *12* (42), 10325−10332.

(38) Dučinskas, A.; Kim, G. Y.; Moia, D.; Senocrate, A.; Wang, Y.-R.; Hope, M. A.; Mishra, A.; Kubicki, D. J.; Siczek, M.; Bury, W.; Schneeberger, T.; Emsley, L.; Milić, J. V.; Maier, J.; Grätzel, M. Unravelling the Behavior of Dion−Jacobson Layered Hybrid Perovskites in Humid Environments. *ACS Energy Lett.* **2021**, *6* (2), 337−344.

(39) García-Espejo, G.; Konidaris, K. F.; Anzini, P.; Brenna, S.; Guagliardi, A.; Masciocchi, N. One and Two-Dimensional 1,4-Xylylenediammonium (pXDA) Lead Halides: Powders and Thin Films. *Eur. J. Inorg. Chem.* **2023**, *26* (23), No. e202300282.

(40) Peng, Y.; Wang, X.; Li, L.; Ye, H.; Yang, S.; Yang, H. G.; Luo, J.; Hou, Y. Moisture-Resistant Chiral Perovskites for White-Light Circularly Polarized Photoluminescence. *Adv. Opt. Mater.* **2023**, *11* (1), 2201888.

(41) Ahn, N.; Kwak, K.; Jang, M. S.; Yoon, H.; Lee, B. Y.; Lee, J.-K.; Pikhitsa, P. V.; Byun, J.; Choi, M. Trapped Charge-Driven Degradation of Perovskite Solar Cells. *Nat. Commun.* **2016**, *7* (1), 13422.

(42) Wu, X.; Sun, S.; Song, T.; Zhang, X.; Wang, C.; Yang, Y.; Wang, S.; Zhong, H. Revealing the Vertical Structure of *in-Situ* Fabricated Perovskite Nanocrystals Films toward Efficient Pure Red Light-Emitting Diodes. *Fundam. Res.* **2024**, *4* (2), 362−368.

(43) Liu, Y.; Lorenz, M.; Ievlev, A. V.; Ovchinnikova, O. S. Secondary Ion Mass Spectrometry (SIMS) for Chemical Characterization of Metal Halide Perovskites. *Adv. Funct. Mater.* **2020**, *30* (35), 2002201.

(44) Bai, Y.; Xiao, S.; Hu, C.; Zhang, T.; Meng, X.; Lin, H.; Yang, Y.; Yang, S. Dimensional Engineering of a Graded 3D−2D Halide Perovskite Interface Enables Ultrahigh Voc Enhanced Stability in the p-i-n Photovoltaics. *Adv. Energy Mater.* **2017**, *7* (20), 1701038.

(45) Sidhik, S.; Wang, Y.; De Siena, M.; Asadpour, R.; Torma, A. J.; Terlier, T.; Ho, K.; Li, W.; Puthirath, A. B.; Shuai, X.; Agrawal, A.;

Traore, B.; Jones, M.; Giridharagopal, R.; Ajayan, P. M.; Strzalka, J.; Ginger, D. S.; Katan, C.; Alam, M. A.; Even, J.; Kanatzidis, M. G.; Mohite, A. D. Deterministic Fabrication of 3D/2D Perovskite Bilayer Stacks for Durable and Efficient Solar Cells. *Science* **2022**, *377* (6613), 1425−1430.

(46) Ilavsky, J.; Jemian, P. R. Irena: tool suite for modeling and analysis of small-angle scattering. *J. Appl. Cryst.* **2009**, *42*, 347−353.

(47) Ilavsky, J. Nika: software for two-dimensional data reduction. *J. Appl. Cryst.* **2012**, *45*, 324−328.

(48) Kresse, G.; Hafner, J. Ab Initio Molecular-Dynamics Simulation of the Liquid-Metal–Amorphous-Semiconductor Transition in Germanium. *Phys. Rev. B* **1994**, *49* (2), 14251−14269.

(49) Kresse, G.; Furthmüller, J. Efficiency of Ab-Initio Total Energy Calculations for Metals and Semiconductors Using a Plane-Wave Basis Set. *Comput. Mater. Sci.* **1996**, *6* (1), 15−50.

(50) Kresse, G.; Joubert, D. From Ultrasoft Pseudopotentials to the Projector Augmented-Wave Method. *Phys. Rev. B* **1999**, *59* (3), 1758−1775.

(51) Kresse, G.; Furthmuller, J. J. Efficient Iterative Schemes for Ab Initio Total-Energy Calculations Using a Plane-Wave Basis Set. *Phys. Rev. B* **1996**, *54* (16), 11169−11186.

(52) Perdew, J. P.; Burke, K.; Ernzerhof, M. Generalized Gradient Approximation Made Simple. *Phys. Rev. Lett.* **1996**, *77* (18), 3865−3868.

(53) Grimme, S.; Ehrlich, S.; Goerigk, L. Effect of the Damping Function in Dispersion Corrected Density Functional Theory. *J. Comput. Chem.* **2011**, *32* (7), 1456−1465.